

## ORIGINAL ARTICLE

# Microstructure-dependent DC set switching behaviors of Ge–Sb–Te-based phase-change random access memory devices accessed by *in situ* TEM

Kyungjoon Baek<sup>1</sup>, Kyung Song<sup>1</sup>, Sung Kyu Son<sup>2</sup>, Jang Won Oh<sup>2</sup>, Seung-Joon Jeon<sup>2</sup>, Won Kim<sup>2</sup>, Ho Joung Kim<sup>2</sup> and Sang Ho Oh<sup>1</sup>

Phase-change random access memory (PCRAM) is one of the most promising nonvolatile memory devices. However, inability to secure consistent and reliable switching operations in nanometer-scale programming volumes limits its practical use for high-density applications. Here, we report *in situ* transmission electron microscopy investigation of the DC set switching of Ge–Sb–Te (GST)-based vertical PCRAM cells. We demonstrate that the microstructure of GST, particularly the passive component surrounding the dome-shaped active switching volume, plays a critical role in determining the local temperature distribution and is therefore responsible for inconsistent cell-to-cell switching behaviors. As demonstrated by a PCRAM cell with a highly crystallized GST matrix, the excessive Joule heat can cause melting and evaporation of the switching volume, resulting in device failure. The failure occurred via two-step void formation due to accelerated phase separation in the molten GST by the polarity-dependent atomic migration of constituent elements. The presented real-time observations contribute to the understanding of inconsistent switching and premature failure of GST-based PCRAM cells and can guide future design of reliable PCRAM.

NPG Asia Materials (2015) 7, e194; doi:10.1038/am.2015.49; published online 26 June 2015

## INTRODUCTION

Phase-change random access memory (PCRAM) devices store and erase information by utilizing a large resistivity difference between the crystalline and amorphous states of chalcogenide materials.<sup>1</sup> Among various chalcogenide materials, the Ge–Sb–Te (GST) alloy system is currently considered the most promising candidate material for PCRAM owing to its fast and reversible phase-transition capability, in both the amorphous-to-crystalline (set) and the reverse crystalline-to-amorphous (reset) switching.<sup>2,3</sup> Moreover, the set switching of GST occurs through an abrupt increase in the current density at a critical electric field, which is known as threshold switching.<sup>1,4</sup> The threshold switching provides local Joule heat and thereby facilitates the crystallization process at a relatively low electric field, ranging from 30 to 50 V  $\mu\text{m}^{-1}$ .<sup>5,6</sup>

Many modern PCRAM cell designs adopt a nanometer-scale hemispherical or cylindrical shape for programming volume to increase the cell density and reduce the operation power.<sup>7</sup> In such device structures, only a portion of the programming volume makes direct contact with a heater electrode, and the other sides are surrounded by passive GST that remains in the crystalline state and acts as an electrical conductivity path during the set and reset switching. One of the critical reliability issues related to these cell structures is the compositional change, or phase separation, caused by electric field-

induced atomic migration.<sup>8</sup> For example, previous studies showed that atomic migration in the molten state of GST is driven by electrostatic forces, resulting in phase separation into a Ge-Sb-rich phase and a Te-rich phase due to the different ionicity of each element.<sup>9</sup> The passive GST component adjacent to the active switching volume is also under the influence of significant Joule heat and the wind force exerted by charge carriers, which potentially causes microstructural or compositional changes during the switching operation.<sup>8,10</sup> A recent study reported that different crystallinity of passive GST component results in different switching behaviors.<sup>10</sup>

To date, major efforts in PCRAM research have been focused on scalability,<sup>11–13</sup> endurance,<sup>13</sup> resistance drift,<sup>14,15</sup> switching speeds and the discovery of new materials.<sup>16</sup> In the case of GST-based PCRAM, the critical issue involves the reliable and durable switching operation of nanometer-scale switching volumes. The inconsistent cell-to-cell switching, material degradation or permanent device failure induced by phase separation in practical PCRAM cells have continuously motivated the need for direct and correlated investigation of the structural transition and electrical switching of individual cells.<sup>10</sup> However, most previous studies have reported only the microstructural and compositional changes that occur after switching, which provide only snapshots of the final states and do not offer a meaningful correlation between electrical switching and structural

<sup>1</sup>Department of Materials Science & Engineering, Pohang University of Science and Technology (POSTECH), Pohang, Republic of Korea and <sup>2</sup>Analysis Team, R&D Division, SK Hynix Semiconductor Inc., Icheon, Republic of Korea

Correspondence: Professor SH Oh, Department of Materials Science & Engineering, Pohang University of Science and Technology (POSTECH), 77 Cheongam-Ro, Nam-Gu, Pohang 790-784, Republic of Korea.

E-mail: shoh@postech.ac.kr

Received 26 July 2014; revised 26 February 2015; accepted 14 April 2015

transitions. *In situ* switching experiment in a transmission electron microscope (TEM) is able to provide a unique solution to this task. However, most *in situ* TEM experiments have been carried out using model structures, for example, suspended bridge or free-standing wire forms of GST.<sup>10,17,18</sup> Although useful, the information obtained from such experiments is not directly applicable to the practical design of PCRAM cells, as the actual current density and associated Joule heat in a confined cell geometry is quite different.

In the present *in situ* TEM study, we directly observed the amorphous-to-crystalline phase transition of GST-based PCRAM cells by applying DC voltages. Although the pulse driven switching is more relevant to understanding what happens during the working conditions of PCRAM devices, it is challenging to investigate detailed structural changes because of the limited time resolution of conventional TEM charge-coupled device cameras (typically 25 fps or 0.04 s). On the other hand, the microstructural changes associated with switching can be observed in greater detail in DC mode, which is the primary focus of the present work. The results show that the initial microstructure of the passive GST component controls the extent of heat confinement in the nanometer-scale switching volume, or the heat dissipated out into the matrix, and thereby critically affects the kinetics of amorphous-to-crystalline phase transitions. Furthermore, the excessive Joule heat induced in the active switching volume surrounded by a highly crystallized GST matrix results in device failure, which was found to occur in a two-step void formation because of the phase separation induced by atomic migration of constituent elements in the molten state of GST.<sup>8</sup> The present results demonstrate that the microstructure of passive GST component is an important parameter that requires precise control during the switching operation of PCRAM devices.

## MATERIALS AND METHODS

### Materials

Conventional vertical PCRAM cells operated with a dome-shaped programming volume with the base diameter of  $\sim 50$  nm were fabricated using a keyhole process followed by deposition/patterning and standard back end-of-line processes.<sup>19</sup> A 100-nm-thick GST thin film was deposited at 473 K by sputtering. The initial state of the as-deposited GST films was amorphous. During the post-growth processes, the film typically undergoes crystallization as the temperature increases up to 623 K, which is well beyond the crystallization temperature of GST. After the growth and patterning of all constituent layers, the active switching volume was formed into a dome shape by applying a reset pulse (1.5 V, 200 ns square pulse with a falling edge of 20 ns). To ensure that the active volume remained in the fully amorphous state, the same reset pulse was applied again to the PCRAM cells before TEM sample preparation.

### Methods

Cross-sectional TEM samples were prepared using a focused ion beam (FIB, Helios NanoLab 450S, FEI Inc., Hillsboro, OR, USA) lift-off technique. The PCRAM cells investigated in the present study were all prepared from the same wafer. The TEM samples were thinned to  $\sim 100$  nm to ensure that the dome-shaped programmed volume was securely contained within the TEM samples. The FIB process parameters were optimized to minimize possible sources of leakage current and open failure of metal electrodes in TEM samples when an electrical bias is applied. Most importantly, to minimize surface damage induced by the high-energy  $\text{Ga}^+$  ion beam, the  $\text{Ga}^+$  ion beam energy was decreased from 30 to 10 keV during the successive FIB milling stages. Then, for the final milling, a low-energy  $\text{Ga}^+$  ion beam was used at 1 keV to remove the surface damage layers. Before *in situ* TEM experiments, the electrical circuit of TEM samples was tested using the nanoprobe system in a secondary electron microscope. This technique can easily screen out the TEM samples that have potential leakage or open failure sources.<sup>20</sup>

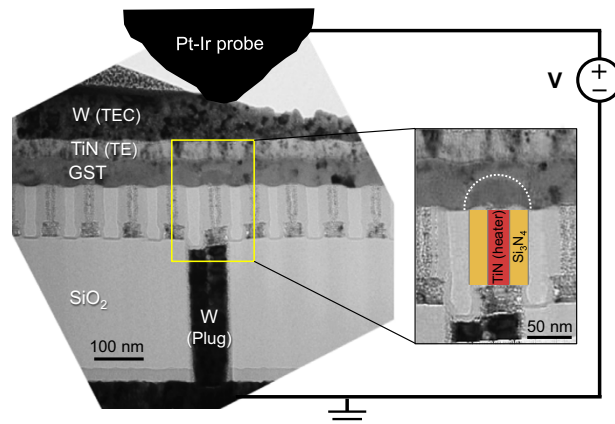


**Figure 1** Cross-sectional transmission electron microscope sample of a vertical phase-change random access memory cell prepared for *in situ* switching. The W plug connected to the TiN heater (highlighted in red) is grounded through attachment to the Cu support grid. A Pt-Ir tip makes electrical contact with the W top electrode contact, constructing an electrical circuit for the application of DC voltage. The TiN heater is surrounded by a thermal/electrical insulator ( $\text{Si}_3\text{N}_4$ , highlighted in yellow). The active switching volume (hemispherical volume) is outlined by a white dotted line.

For *in situ* TEM switching experiments, the Pt-Ir probe installed in the TEM holder (STM-TEM holder, Nanofactory Inc., Gothenburg, Sweden) was put into direct contact with the W top electrode (refer to Figure 1). The TiN bottom electrode that serves as the local heater was connected to an electrically grounded Cu support grid via the W plug. The set switching of PCRAM was driven by applying a DC voltage from 0 to 1.5 V at a constant ramping rate of  $10 \text{ mV s}^{-1}$ . The DC current was measured at a sampling rate of  $\sim 20 \text{ s}^{-1}$  during the observation of microstructural changes in real-time (25 fps). The measured  $I$ - $V$  curves were correlated with the simultaneously recorded real-time TEM movies and used to evaluate the characteristic switching behaviors of individual PCRAM cells. *In situ* TEM experiments were carried out using a field-emission TEM (JEM-2100F, JEOL Ltd., Tokyo, Japan) operated at 200 kV. The diffraction contrast in conventional bright-field TEM mode was used to observe the detailed switching process.

### Characterization

To calculate the temperature distribution in a PCRAM cell during the DC set switching, finite element modeling (FEM) was carried out using COMSOL Multiphysics (COMSOL Inc., Burlington, MA, USA). In general, the temperature distribution in a device is determined by local Joule heat generated by the current flowing along a conducting substance and its conduction to surrounding materials. The temperature distribution is calculated by solving the following heat conduction equation:

$$\frac{j^2}{\sigma} + \nabla \cdot k \nabla T = \rho C_p \frac{\partial T}{\partial t} \quad (1)$$

Here,  $C_p$  is the specific heat,  $\rho$  is the density,  $t$  is the time,  $T$  is the temperature,  $k$  is the thermal conductivity,  $\sigma$  is the electrical conductivity and  $j$  is the current density. The cell geometry constructed for FEM is detailed in Figure 2a, and the material properties are summarized in Table 1.<sup>21–23</sup> According to Equation (1), the amount of heat generated within the switching volume of PCRAM is predominantly determined by the actual  $\sigma$  and  $k$  values of GST. Although the  $k$  value of GST shows a relatively small variation, in the range of 0.2–0.5  $\text{W m}^{-1} \text{K}^{-1}$ ,<sup>21</sup> the  $\sigma$  value varies drastically with the crystallinity of GST, varying from 0.5 to 2770  $\text{S m}^{-1}$ .<sup>21</sup> Thus, the crystallinity-dependent electrical conductivity,  $\sigma$ , of GST is the major factor that determines the temperature distribution and the maximum temperature ( $T_{\text{max}}$ ) in the active switching volume.

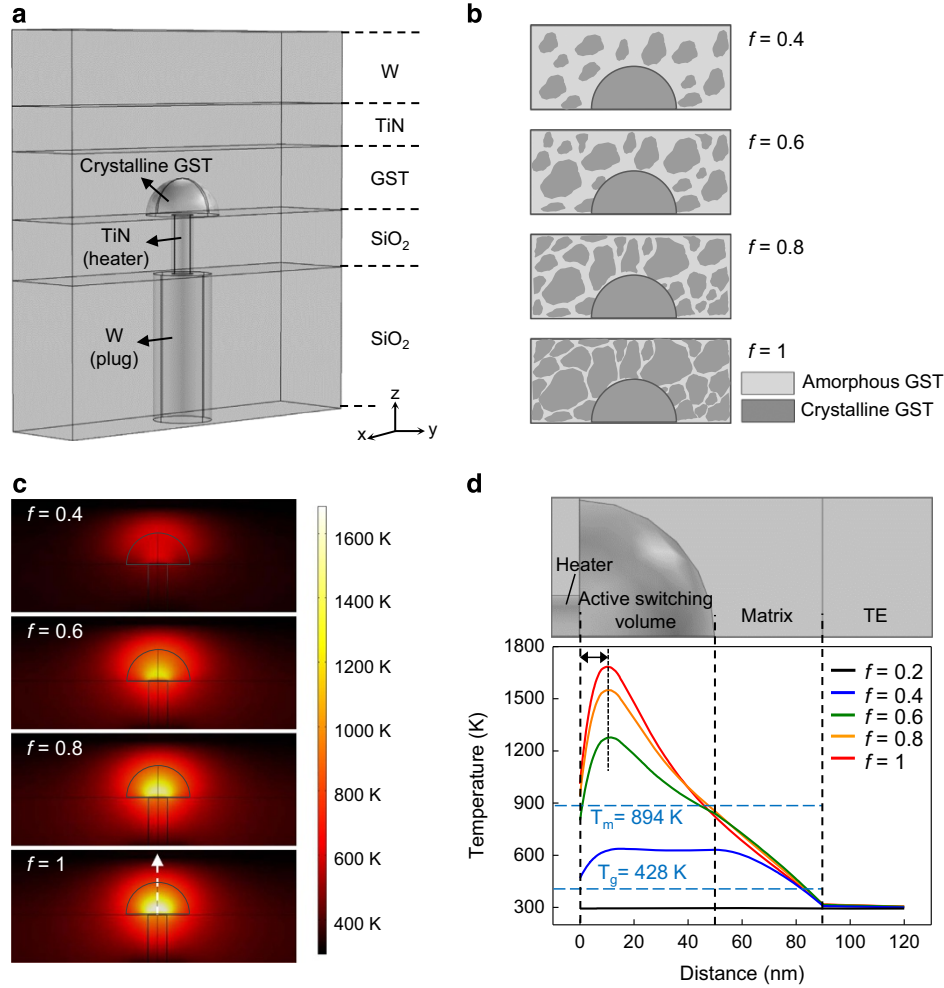


**Figure 2** Finite element modeling calculation of temperature distribution in the active switching region at 1.4 V during memory swathing. **(a)** Schematic representation of model device structure. The dimension of the W and TiN top electrode are  $500 \times 120 \times 100 \text{ nm}^3$  and  $500 \times 120 \times 60 \text{ nm}^3$ , respectively. The Ge-Sb-Te layer dimensions are  $500 \times 120 \times 90 \text{ nm}^3$ , in which the switching volume is defined as a hemisphere with the base radius of 50 nm over TiN heater. The TiN heater has a cylindrical shape with a radius of 15 nm and a height of 80 nm. The W plug is located just below the TiN heater, which has a cylindrical shape with a radius of 40 nm and a height of 200 nm. The TiN heater and the W plug are surrounded by SiO<sub>2</sub>. **(b)** Schematic illustration of phase-change random access memory cells with different degrees of crystallinity ( $f$ ). In the simulation, the active switching volume was treated as a crystalline phase (i.e.,  $f = 1$ ) whereas the matrix crystallinity was varied from 1 to 0.4. Other material parameters used for the simulation are given in Table 1. **(c)** Temperature maps with varied  $f$  values. **(d)** Temperature profile across the programming volume of each cell with different  $f$  values (along a white dotted arrow in **c**). The crystallization temperature ( $T_g = 428 \text{ K}$ ) and the melting point ( $T_m = 894 \text{ K}$ ) of Ge-Sb-Te are indicated in the plot. The interface offset distance of  $T_{\text{max}}$  from the TiN heater is indicated by a black arrow.

We applied Equation (1) to PCRAM cells that are switched to the set state at the DC voltage of 1.4 V. Under this condition, the switching volume can be treated as in the crystalline state. Then, the GST matrix crystallinity ( $f$ ) was selected as an adjustable structural parameter to account for varied cell crystallinity;<sup>24,25</sup> for fully amorphous and crystalline states,  $f$  corresponds to 0 and 1, respectively, and for an intermediate state,  $f$  ranges between 0 and 1. The  $k$  and  $\sigma$  values of GST vary in proportion to  $f$ , according to the following:

$$\sigma(f, \sigma_a, \sigma_c) = \frac{1}{4} \left[ 2\sigma_p - \sigma_p' + \sqrt{(2\sigma_p - \sigma_p')^2 + 8\sigma_a\sigma_c} \right], \quad (2)$$

with  $\sigma_p = (1-f)\sigma_a + f\sigma_c$  and  $\sigma_p' = f\sigma_a + (1-f)\sigma_c$ .  $\sigma_a$  and  $\sigma_c$  are the electrical conductivities of bulk amorphous and crystalline phases, respectively.<sup>24</sup> This relationship is based on the random configurations of spherical crystalline clusters, such as the Bruggeman-type effective medium,<sup>25</sup> and this approximation is also applied to the thermal conductivity,  $k$ . Typical values of  $\sigma$  and  $k$  with varied degrees of  $f$  adopted in the FEM are summarized in Table 1. The model cell structures with various  $f$  values, that is, the different degrees of GST matrix crystallinity, are schematically presented in Figure 2b. The temperature and

voltage were initially set to 298 K and 0 V, respectively. The top surface of the W top electrode and the bottom surface of the W plug were fixed at 298 K, and DC voltage was applied to the former while the latter was electrically grounded. All other exterior surfaces were set as thermally and electrically insulating.

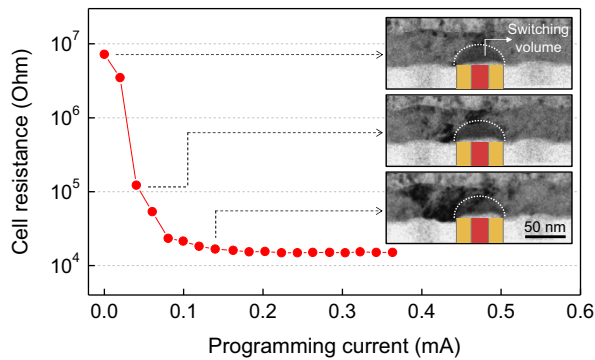
## RESULTS AND DISCUSSION

Figure 1 shows the cross-sectional TEM image of a PCRAM device prepared for set switching in TEM. The schematic representation illustrates the DC voltage application to the active switching volume through the Pt-Ir probe. Each cross-sectional TEM specimen contains a series of PCRAM cells, of which only the center cell, highlighted in yellow (for Si<sub>3</sub>N<sub>4</sub>) and red (TiN heater), is connected to the W plug and thus switchable. Given that the active switching volume (outlined by white dotted line in the Figure 1 inset) was initially at the reset state, the DC current flowing through the entire circuit is limited by the amorphous GST of the switching volume. The reset resistance of

**Table 1** Electrical ( $\sigma$ ) and thermal ( $k$ ) conductivity of the materials used in FEM

Materials	Electrical conductivity, $\sigma$ ( $S m^{-1}$ )	Thermal conductivity, $k$ ( $W m^{-1} K^{-1}$ )
SiO <sub>2</sub>	$1 \times 10^{-7}$	1.4
W	$6 \times 10^6$	174
TiN	$1 \times 10^6$	13
GST ( $f=0.0$ )	0.5	0.2
GST ( $f=0.2$ )	1.25	0.24
GST ( $f=0.4$ )	279	0.29
GST ( $f=0.6$ )	1108	0.36
GST ( $f=0.8$ )	1939	0.42
GST ( $f=1.0$ )	2770	0.5

Abbreviations: FEM, finite element modeling; GST, Ge-Sb-Te. In case of GST,  $\sigma$  and  $k$  varies from 0.5 to 2770 and from 0.2 to 0.5, respectively, depending on the crystallinity.  $f$  is defined to take different GST crystallinities into account.<sup>25</sup> For example,  $f$  for fully amorphous and crystalline states corresponds to 0 and 1, respectively, and for an intermediate state  $f$  ranges between 0 and 1.



**Figure 3** Change of the cell resistance and microstructure of a phase-change random access memory cell during DC set switching in transmission electron microscope. Note that the Ge-Sb-Te matrix surrounding the active switching volume is subject to structural changes while the switching volume undergoes set switching by an amorphous-to-crystalline phase transition. The cell resistance was changed by approximately three orders of magnitude as a result of set switching. The active switching volume is outlined by a white dotted line.

all PCRAM cells was in the similar order of magnitude ( $10 M\Omega$ ), as the example shown in Figure 3.

Ideally, the DC set switching of standard PCRAM cells of the current design occurs through an abrupt increase in the current density with the onset of threshold switching at the critical voltage of  $\sim 1.3$  V, which provides local Joule heat that crystallizes the amorphous switching volume in the memory-switching regime. However, the switching behaviors of individual cells on the same wafer were often different from cell to cell, and some of them showed an early failure, which we refer to as inconsistent switching. Here, we focus on the switching behaviors of two types of PCRAM cells, one representing normal cells that show a clear threshold switching and subsequent stable memory switching (cell A, shown in Figure 4a) and the other exhibiting direct memory switching without threshold switching and an early failure at the voltages where a normal cell would exhibit stable memory switching (cell B, shown in Figure 4b).

When the initial microstructures of cells A and B are compared, there is no notable difference in the active switching region. However, the microstructure of the passive GST component surrounding the

active switching volume is greatly different between the two cells; while the cell A matrix consists of small grains exhibiting relatively weak diffraction contrast in the TEM image (Figure 4a), cell B contained well-crystallized coarse grains exhibiting strong diffraction contrast (Figure 4b). Here the ‘matrix’ is referred to as the region surrounding the active switching volume boundary to about 50 nm, which is usually subjected to microstructural changes due to heat conduction from the switching volume. The crystallization of GST matrix takes place during both the post-growth processes and the set and reset switching, as shown in Figure 3, as a result of local conduction of Joule heat toward the matrix. These heat effects vary from cell to cell and are almost impossible to control precisely on a cell basis. Thus, the GST matrix microstructure and crystallinity differs slightly in different cells, which we consider one possible cause of inconsistent switching. In the case of cell B, we postulate that the local thermal input is larger than average, which results in the formation of large grains in the GST matrix. We used the grain size as a quantitative measure of the crystallinity of GST matrix. Figure 4c shows the distribution of grain size in cells A and B, which was measured from TEM images. The average grain sizes of cells A and B were measured at 12.27 and 16.28 nm, respectively.

Hereafter we focus on the microstructural evolution of cells A and B during DC set switching. The microstructural evolution of the active switching region of cell A was characterized in correlation with the log-plotted  $I$ - $V$  curve and summarized in Figure 5 (see Supplementary Movie 1). The  $I$ - $V$  curve can be divided into three regimes: (1) amorphous-off; (2) threshold switching and; (3) memory switching (Figures 5a and b). In the amorphous-off regime, the current remained as low as 0.1 mA, and no structural changes were observed in the corresponding TEM images, for example, Figure 5c. The amorphous-off regime is divided into two sub-regimes which show different voltage-dependency of current, that is,  $\ln I \propto \sqrt{V}$  from 0 to 0.4 V, and then  $\ln I \propto V$  from 0.4 to 1.15 V. The observed current-voltage dependencies can be attributed to the typical conduction behaviors of amorphous GST, which follows the Poole-Frenkel conduction mechanism.<sup>26</sup>

With the onset of threshold switching in cell A, the DC current increases steeply at  $\sim 1.15$  V. While the current increased linearly as a whole, it showed repeated drops during threshold switching. However, the microstructure of the switching volume remained almost the same as the initial amorphous state without noticeable changes (Figure 5d). It was only after the onset of memory switching at 1.4 V, when the nucleation of crystalline phase is discernible in the TEM diffraction contrast (indicated by red arrow in Figure 5e). The memory switching is distinguished clearly by a change in the slope of the  $I$ - $V$  curve in Figure 5b and the concurrent appearance of nanometer-sized crystalline phases at  $\sim 1.4$  V in Figure 5e.

Regarding the threshold switching mechanism, the present results cannot unambiguously resolve the controversy between two competing models,<sup>27</sup> that is, the formation of conductive crystalline filaments<sup>28</sup> or an accelerated electrical transition via trap levels.<sup>29</sup> The detection of conductive filaments by TEM is very challenging in such an embedded cell geometry because of the two-dimensional projection nature of TEM images. Considering the spatial resolution ( $\delta$ ) of TEM diffraction contrast imaging,  $\delta \approx 0.61\lambda/\alpha = 0.8$  nm, where  $\lambda$  and  $\alpha$  are the wavelength (0.00251 nm) and the convergent angle (3.125 mrad) of the electron beam, respectively, critical nuclei or conductive filaments are in principle detectable (the radius of a critical nucleus is typically 1–3 nm<sup>30,31</sup>). However, the two-dimensional projection nature of TEM imaging limits the smallest detectable size

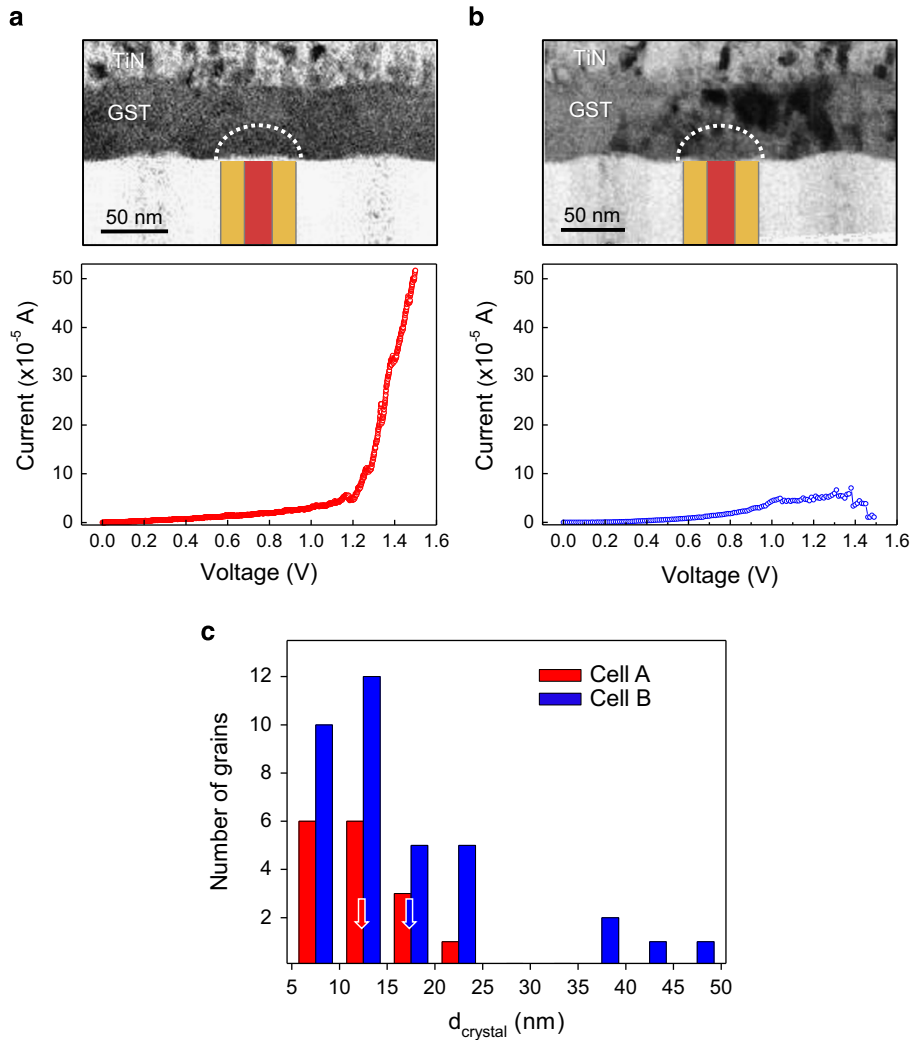


**Figure 4** Two representative phase-change random access memory cells with different switching behaviors. (a) A cell exhibiting normal memory switching via threshold switching (cell A) and (b) a cell showing early failure after direct memory switching (cell B). The initial microstructure and  $I$ - $V$  curve obtained during *in situ* transmission electron microscopy switching are shown for each cell. (c) Grain size distribution in the Ge-Sb-Te matrix of cells A and B. The average grain sizes of cells A and B were 12.27 and 16.28 nm, respectively.

of crystals embedded within TEM samples of  $\sim 100$  nm to  $\sim 6$  nm thickness.

In the memory-switching regime, nucleation and growth of the crystalline phase was detected not only in the programmable volume but also in the surrounding GST matrix (arrows in Figures 5e-g), indicating that the heat-affected zone is extended beyond the switching volume. Using high-resolution TEM (HRTEM), we confirmed that the dark contrast detected in the conventional TEM images is indeed the crystalline phase of GST. Figure 6 shows a HRTEM image and fast Fourier transformation pattern of one of the crystalline phases. The measured  $d$ -spacing of the lattice fringes (region b in Figure 6a and Figure 6b) is  $\sim 0.30$  nm, which corresponds to the (200) plane spacing of the face-centered cubic phase of GST.<sup>32,33</sup> The neighboring GST matrix also revealed the lattice fringes and corresponding diffraction spots in the fast Fourier transformation (region c in Figure 6a and Figure 6c), but the contrast was relatively weak.

To avoid electron beam irradiation effects, the current density of the 200 kV-electron beam was kept as low as  $0.3 \text{ nA } \mu\text{m}^{-2}$  (equivalent to the electron dose rate of  $2.2 \times 10^3 \text{ electrons } \mu\text{m}^{-2}\text{s}^{-1}$ ) throughout the

*in situ* TEM experiments. In addition, to ensure that the surrounding matrix changes were not caused by electron beam irradiation,<sup>34</sup> we performed control DC switching experiments with the electron beam being turned off.<sup>10,35</sup> The measured  $I$ - $V$  curve and correlating TEM images before and after DC set switching are provided in the Supplementary Information (Supplementary Figure S1). The DC switching behavior and associated structural change of the surrounding matrix observed in the control experiment (beam off condition) was essentially identical to those observed *in situ* with the beam on; the crystallization of the surrounding GST matrix is caused by heat conduction from the active switching volume, not by electron irradiation effects.

In cell B, the nucleation of crystalline phase occurred directly without threshold switching. As shown in Figure 7 (see also Supplementary Movie 2), the nucleation of crystalline phase occurred at the hot spot above the TiN heater at a much lower voltage (0.97 V) than the typical threshold voltage ( $\sim 1.3$  V). Note that the log-plotted  $I$ - $V$  curve of this cell showed a similar voltage dependency to that of cell A in the amorphous-off regime, that is, initially  $\ln I \propto \sqrt{V}$  and

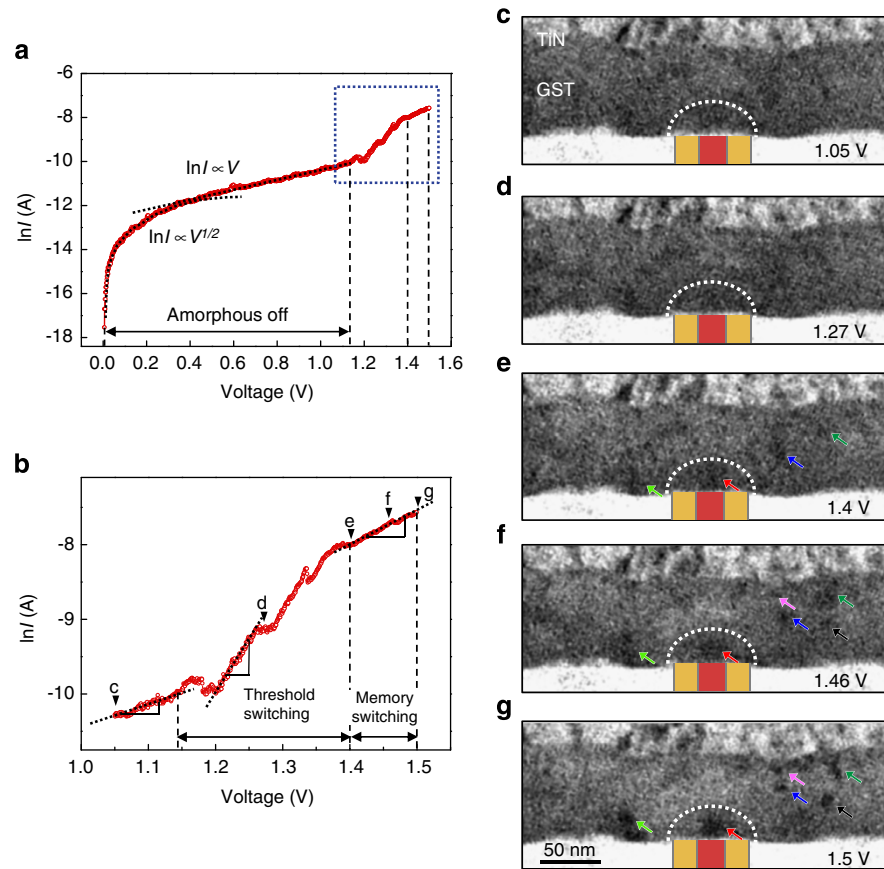


**Figure 5**  $I$ - $V$  characteristics and correlated microstructural evolutions of cell A. (a)  $I$ - $V$  curve plotted in log-scale. The  $I$ - $V$  curve is divided into three regimes: amorphous-off (0–1.15 V); threshold switching (1.15–1.4 V); and memory switching (1.4–1.5 V). (b) Detailed view of the threshold and memory-switching regimes outlined by a blue dotted line in (a). (c–g) transmission electron microscopy images corresponding to the points indicated in (b). The microstructure of the active switching volume remained nearly the same as that of the initial state until the voltage increased to 1.4 V, at which memory switching occurs with the appearance of a crystalline phase. The crystalline phase appears as nano-particles in the active switching volume and in the matrix.

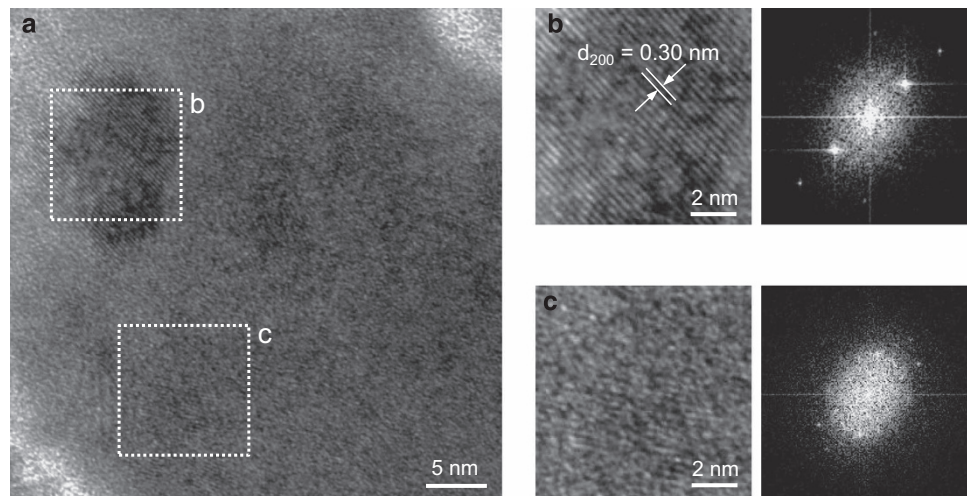


**Figure 6** High-resolution transmission electron microscopy image of the crystalline phase. (a) High-resolution transmission electron microscopy image of the Ge-Sb-Te matrix of cell A containing the nucleated crystalline phase after DC set switching. The crystalline phase (indicated by region b) is embedded as nanoparticles in the matrix (region c). (b) Enlarged high-resolution transmission electron microscopy image of region b and the corresponding fast Fourier transformation pattern. The measured  $d$ -spacing of  $\sim 0.30$  nm coincides with that of the Ge-Sb-Te (200) plane. (c) Enlarged high-resolution transmission electron microscope image of region c and the corresponding fast Fourier transformation pattern showing relatively low crystallinity.

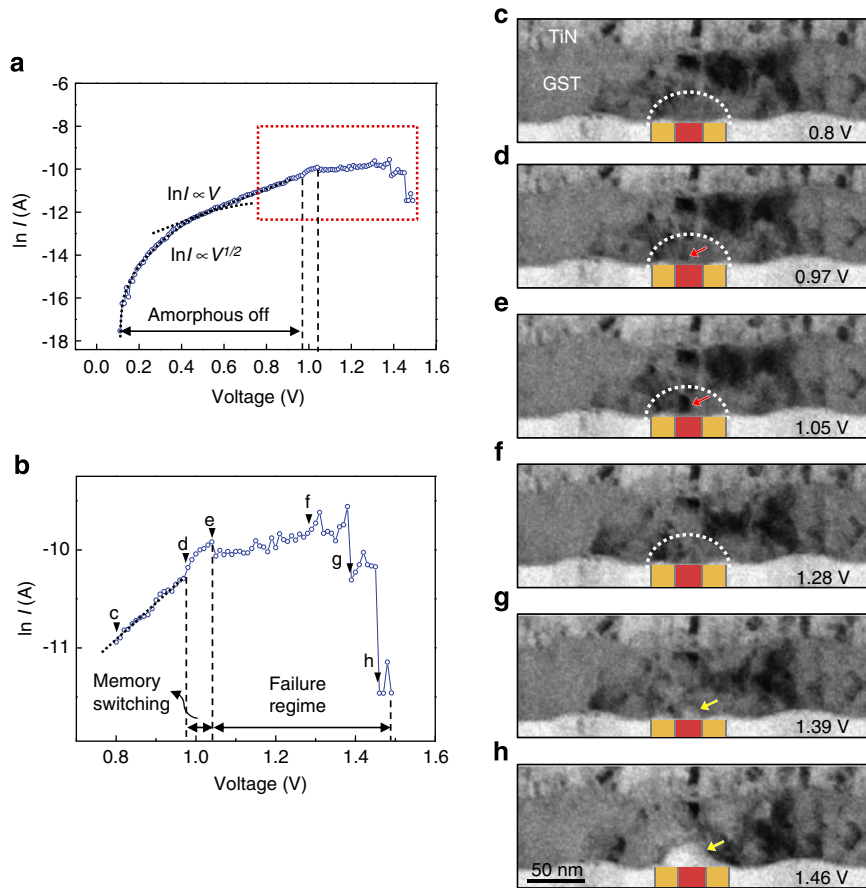


**Figure 7**  $I$ - $V$  characteristics and correlated microstructural evolutions of cell B. (a)  $I$ - $V$  curve plotted in log-scale. The  $I$ - $V$  curve is divided into three stages: amorphous-off (0–0.97 V), memory switching (0.97–1.05 V) and failure (1.05–1.5 V). (b) Detailed view of the memory-switching and failure regimes of the  $I$ - $V$  curve outlined by red dotted line in a. (c–h) Transmission electron microscopy images corresponding to the points indicated in b. The stable crystalline phase appeared at 0.97 V (point d) and grew (point e) in the hot spot of the switching volume. At 1.39 V (point g), a void appeared at the central region of the active switching volume with a current drop of  $\sim 0.04$  mA. The second current drop occurred at 1.46 V with complete failure of the switching volume.

then  $\ln I \propto V$  at higher voltages (Figure 7a). As soon as the nucleation occurred in the active switching volume, the  $I$ - $V$  curve slope deviates from the  $\ln I \propto V$  relationship and increases more steeply (from points d to e in Figure 7b), entering the memory-switching regime. Although the crystalline phase grew during memory switching (red arrows in Figures 7d and e), the adjacent GST matrix also underwent structural changes, indicating that the heat-affected zone in this cell extends beyond the switching volume and induces substantial microstructural changes in the surrounding matrix.

The size of crystalline phase ( $d_{\text{crystal}}$ ) formed at different locations was measured and plotted as a function of the applied voltage (Figures 8a and b). The plot shows that the growth rate of the crystal within the switching volume was much higher than that of other crystals (Figure 8a). Careful measurements through TEM intensity profiling reveal that this crystalline phase formed a few nanometers away from the TiN heater/GST interface (Figures 8a and b). The interface offset distance was 6 and 8 nm for samples A and B, respectively.

PCRAM cells that undergo direct memory switching without threshold switching become unstable at higher voltages. As represented by cell B, continued increases in DC voltage after memory switching resulted in repeated current fluctuations (maximum peak-to-peak variation of  $\pm 0.01$  mA, as shown in Figure 7b). The correlated TEM movie demonstrates that this instability is caused by local

melting of the switching volume (Supplementary Movie 2). A void was formed in the central region of the switching volume (yellow arrow in Figure 7g) and was accompanied by an abrupt current drop ( $\sim 0.04$  mA) at  $\sim 1.39$  V. At 1.46 V, a second current drop ( $\sim 0.03$  mA) occurred with complete failure of the remaining switching volume (yellow arrow in Figure 7h). This result shows that the failure of the GST switching volume occurs through a two-step void formation and is probably due to phase separation in the molten GST under a high current density.

FEM demonstrate that the different switching behaviors of the PCRAM cells in these studies are most likely caused by different extents of heat concentration/conduction, which are dependent upon the GST matrix crystallinity. Figure 2c shows temperature maps calculated with different GST matrix crystallinities,  $f$ . The results clearly show that the Joule heat becomes more strongly confined to the switching volume as the crystallinity increases, resulting in a higher  $T_{\text{max}}$  in the switching volume (Figure 2c). This result indicates that at a given DC voltage, the  $T_{\text{max}}$  in cell B is always greater than that of cell A, and thus the memory switching can occur at a lower voltage in cell B (0.97 V) than in cell A (1.4 V). Figure 2d shows the temperature profiles obtained along the vertical direction from the TiN/GST interface to the top electrode (white dotted arrow in Figure 2c). The  $T_{\text{max}}$  of the switching volume can reach the melting temperature of GST ( $T_m \sim 894$  K<sup>36</sup>) when  $f$  is greater than 0.6, suggesting that melting

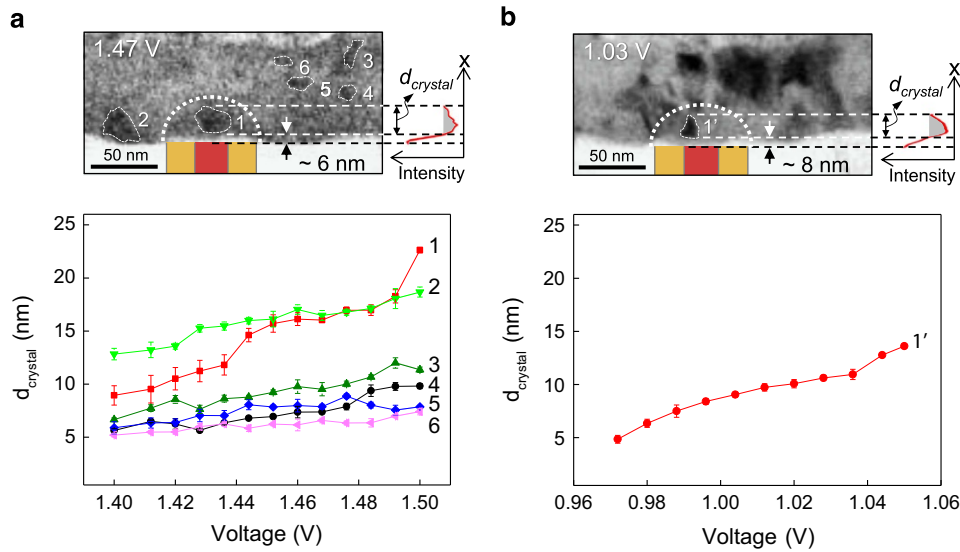


**Figure 8** Growth of the crystalline Ge-Sb-Te phase during memory switching. The size of the crystalline Ge-Sb-Te phase was measured and plotted as a function of DC voltage in (a) cell A and (b) cell B. The size of the smallest detectable crystal by transmission electron microscopy was  $\sim 6$  nm. In cell A, the crystalline phase was also formed outside the active switching volume. The onset voltage of memory switching was different in the two cells, i.e., 1.4 V in cell A and 0.97 V in cell B. The interface offset distance of the crystalline phase formed within the active switching volume was measured by intensity profiling of the transmission electron microscopy images to be  $\sim 6$  and  $\sim 8$  nm for cells A and B, respectively.

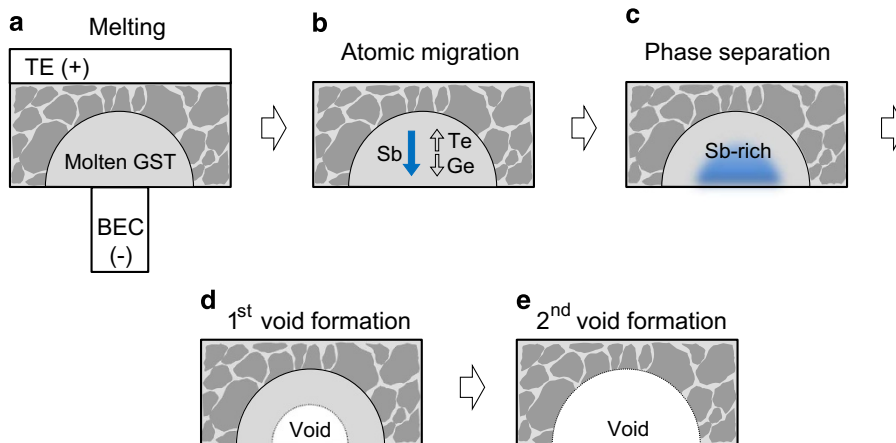


**Figure 9** A model proposed for the failure of phase-change random access memory by two-step void formation. (a) Melting of Ge-Sb-Te in the active switching volume encompassed by a high-crystalline Ge-Sb-Te. (b) Mass redistribution in the Ge-Sb-Te melt driven primarily by electrostatic forces, which results in phase separation. Among the constituent elements, Sb ions migrate toward the bottom electrode contact (BEC) much faster than the other ions. (c) Formation of a Sb-rich phase near the BEC. (d) First void formation at the central region (corresponding to the hottest spot) by the preferential evaporation of the Sb-rich phase. (e) Second void formation of the remaining Ge-Sb-Te melt leading to complete mass loss of the switching volume.

and evaporation can occur in a switching volume that is surrounded by a highly crystalline GST matrix.

When assessing the spatial distribution of temperature,  $T_{\max}$  appears a few nanometers away from the TiN/GST interface in the simulations (arrow in Figure 2d). This result is attributable to an improved thermal conduction pathway through TiN that increases local heat dissipation at the TiN/GST interface. This result agrees with the preferential nucleation site determined by *in situ* TEM (Figure 8), which is located  $\sim 6$ – $8$  nm above the interface. The heat-affected zone extends beyond the hemispherical switching volume to  $\sim 40$  nm. In this region, temperature increases to well above the GST crystallization temperature ( $T_g \sim 428$  K<sup>36</sup>), except when  $f < 0.2$ . This result suggests that the GST matrix in this region is subject to microstructural

changes, such as the nucleation (as observed in cell A) and/or the grain growth of crystalline phase (cell B), which in turn affect the heat confinement in the switching volume.

The two-step void formation can be accounted for by the phase-separation (or mass-redistribution) model of GST. According to previous studies, the atomic migration activating in GST are dependent on temperature, current density and material state, which results in phase separation into different end products at different locations.<sup>37</sup> Based on our real-time observations, we propose a model for the two-step void formation, schematically illustrated in Figure 9. First, we ensured that the observed two-step void formation took place in the ‘molten state’ of GST (Figure 9a). This hypothesis is supported by direct TEM observation of the constant fluctuation of diffraction



contrast, indicating GST melting (Supplementary Movie 2) and by FEM showing that temperature increases to above the melting point (Figure 2). The current density at which the void formation took place was on the order of  $10^6 \text{ A cm}^{-2}$ . Therefore, atomic migration under such a high current density is primarily driven by the 'electrostatic force' acting on the constituent elements of molten GST, which results in the formation of a Sb-rich phase near the bottom electrode contact (BEC). The average value of  $DZ^*$  ( $D$  is the diffusion coefficient and  $Z^*$  is the effective charge number) of Ge, Sb and Te are calculated to be 1.13, 1.98, and  $-1.17 \times 10 \text{ cm}^2 \text{ s}^{-1}$ , thus, the diffusion velocity of Sb is  $\sim 1.7$  times faster than those of Ge and Te in molten GST<sup>9</sup> (Figure 9b). If the atomic migration was driven by the wind force of charge carriers, all elements of GST would migrate in the same direction.<sup>9</sup> Given that the diffusion of Sb ions is much faster than that of Ge ions, the Sb-rich phase that forms near the BEC (Figure 9c) probably has a lower evaporation temperature or equivalently higher equilibrium vapor pressure than that of the Te-rich phase. In the Ge-Te-Sb ternary phase diagram, a Sb-rich phase has a lower melting point,<sup>38,39</sup> so that its equilibrium vapor pressure is likely to be higher than that of the Te-rich phase. Moreover, the temperature profile shows that the temperature where the Sb-rich phase is located near the BEC (that is, hot spot) is much higher than that of the Te-rich phase. All of these considerations favor the formation and preferential evaporation of the Sb-rich phase near the BEC (Figure 9d). Then, the remaining region of switching volume undergoes evaporation with increased voltage, and the cell fails completely (Figure 9e).

## CONCLUSIONS

In summary, direct observations of the DC set switching process and the supporting FEM simulations on temperature distribution demonstrate that the crystallinity of surrounding GST matrix influences the heat distribution in the active switching volume of vertical PCRAM cells. The FEM calculations show that at a given DC voltage, the temperature of active switching volume increases with the surrounding GST matrix crystallinity. The microstructure of GST matrix is continuously evolving during the set and reset switching because of heat conduction from the active switching volume. The FEM predicts that the heat-affected zone extends to  $\sim 40 \text{ nm}$  from the boundary of the switching volume. In the case of a highly crystallized GST matrix, the temperature increases to above the melting point of GST, which leads to device failure via two-step void formation due to phase separation that is accelerated by atomic migration in molten GST. The present results contribute to the current understanding on inconsistent switching and long-term reliability of PCRAM cells and provide useful information for optimizing the design of future PCRAM devices. For example, in vertical PCRAM cell designs one has to consider a way to suppress heat conduction to minimize microstructural changes in the GST matrix surrounding the active switching volume.

## CONFLICT OF INTEREST

The authors declare no conflict of interest.

## ACKNOWLEDGEMENTS

This research was supported by the Pioneer Research Center Program through the National Research Foundation (NRF) of Korea funded by the Ministry of Science, ICT & Future Planning (no. 2012-0009460); the NRF grant funded by the Korea government (no. 2012K2A1A9054818); and the Brain Korea 21 PLUS project for the Center for Creative Industrial Materials.

*Author contributions:* SHO conceived the study, designed the experiments and wrote the manuscript. KB and KS performed the *in situ* TEM experiments, analyzed the data and wrote the manuscript under the supervision of SHO. KB

carried out the finite element modeling. SKS, JWO, SJJ and WK fabricated the vertical PCRAM devices and prepared the TEM samples. SHO, KB, KS and SJJ discussed the data interpretation and revised the manuscript.

- 1 Wuttig, M. & Yamada, N. Phase-change materials for rewriteable data storage. *Nat. Mater.* **6**, 824–832 (2007).
- 2 Loke, D., Lee, T. H., Wang, W. J., Shi, L. P., Zhao, R., Yeo, Y. C., Chong, T. C. & Elliott, S. R. Breaking the speed limits of phase-change memory. *Science* **336**, 1566–1569 (2012).
- 3 Kohara, S., Kato, K., Kimura, S., Tanaka, H., Usuki, T., Suzuya, K., Tanaka, H., Moritomo, Y., Matsunaga, T., Yamada, N., Tanaka, Y., Suematsu, H. & Takata, M. Structural basis for the fast phase change of  $\text{Ge}_2\text{Sb}_2\text{Te}_5$ ; ring statistics analogy between the crystal and amorphous states. *Appl. Phys. Lett.* **89**, 201910 (2006).
- 4 Ovshinsky, S. R. Reversible electrical switching phenomena in disordered structure. *Phys. Rev. Lett.* **21**, 1450–1453 (1968).
- 5 Wright, C. D., Armand, M. & Aziz, M. M. Terabit-per-square-inch data storage using phase-change media and scanning electrical nanoprobes. *IEEE Trans. Nanotechnol.* **5**, 50–61 (2006).
- 6 Lankhorst, M. H., Ketelaars, B. W. & Wolters, R. Low-cost and nanoscale non-volatile memory concept for future silicon chips. *Nat. Mater.* **4**, 347–352 (2005).
- 7 Raoux, S., Burr, G. W., Breitwisch, M. J., Rettner, C. T., Chen, Y. C., Shelby, R. M., Salinga, M., Krebs, D., Chen, S.-H., Lung, H. L. & Lam, C. H. Phase-change random access memory: a scalable technology. *IBM J. Res. Dev.* **52**, 465–479 (2008).
- 8 Nam, S. W., Lee, D., Kwon, M. H., Kang, D., Kim, C., Lee, T. Y., Heo, S., Park, Y. W., Lim, K., Lee, H. S., Wi, J. S., Yi, K. W., Khang, Y. & Kim, K. B. Electric-field-induced mass movement of  $\text{Ge}_2\text{Sb}_2\text{Te}_5$  in bottleneck geometry line structures. *Electrochem. Solid-State Lett.* **12**, H155–H159 (2009).
- 9 Yang, T. Y., Park, I. M., Kim, B. J. & Joo, Y. C. Atomic migration in molten and crystalline  $\text{Ge}_2\text{Sb}_2\text{Te}_5$  under high electric field. *Appl. Phys. Lett.* **95**, 032104 (2009).
- 10 Meister, S., Kim, S., Cha, J. J., Wong, H. S. P. & Cui, Y. *In situ* transmission electron microscopy observation of nanostructural changes in phase-change memory. *ACS Nano* **5**, 2742–2748 (2011).
- 11 Hamann, H. F., O'Boyle, M., Martin, Y. C., Rooks, M. & Wickramasinghe, K. Ultra-high-density phase-change storage and memory. *Nat. Mater.* **5**, 383–387 (2006).
- 12 Milliron, D. J., Raoux, S., Shelby, R. & Jordan-Sweet, J. Solution-phase deposition and nanopatterning of GeSbSe phase-change materials. *Nat. Mater.* **6**, 352–356 (2007).
- 13 Lee, S. H., Jung, Y. & Agarwal, R. Highly scalable non-volatile and ultra-low power phase-change nanowire memory. *Nat. Nanotechnol.* **2**, 626–630 (2007).
- 14 Pirovano, A., Lacaíta, A. L., Pellizzer, F., Kostylev, S. A., Benvenuti, A. & Bez, R. Low-field amorphous state resistance and threshold voltage drift in chalcogenide materials. *IEEE Trans. Electron. Devices* **51**, 714–719 (2004).
- 15 Ielmini, D., Lacaíta, A. L. & Mantegazza, D. Recovery and drift dynamics of resistance and threshold voltages in phase-change memories. *IEEE Trans. Electron. Devices* **54**, 308–315 (2007).
- 16 Hong, S. H., Bae, B. J. & Lee, H. Fast switching behavior of nanoscale  $\text{Ag}_6\text{In}_5\text{Sb}_{59}\text{Te}_{30}$  based nanopillar type phase change memory. *Nanotechnology* **21**, 025703 (2010).
- 17 Nam, S. W., Chung, H. S., Lo, Y. C., Qi, L., Li, J., Lu, Y., Johnson, A. T. C., Jung, Y., Nukala, P. & Agarwal, R. Electrical wind force-driven and dislocation-templated amorphization in phase-change nanowires. *Science* **336**, 1561–1566 (2012).
- 18 Nukala, P., Agarwal, R., Qian, X., Jang, M. H., Dhara, S., Kumar, K., Johnson, A. T. C., Li, J. & Agarwal, R. Direct observation of metal-insulator transition in single-crystalline germanium telluride nanowire memory devices prior to amorphization. *Nano Lett.* **14**, 2201–2209 (2014).
- 19 Lee, M. H., Cheek, R., Chen, C. F., Zhu, Y., Bruley, J., Baumann, F. H., Shih, Y. H., Lai, E. K., Breitwisch, M., Schrott, A., Raoux, S., Joseph, E. A., Cheng, H. Y., Wu, J. Y., Lung, H. L. & Lam, C. The impact of hole-induced electromigration on the cycling endurance of phase change memory. *IEEE IEDM Tech. Dig.* **28**, 1–4 (2010).
- 20 Son, S. K., Jeon, S. J., Oh, J. W., Kim, W., Kim, H. J., Lee, J. H., Woo, S. H., Do, G. S., Lee, S. Y., Baek, K. J. & Oh, S. H. In-situ characterization of switching mechanisms in phase change random access memory (PRAM) using transmission electron microscopy (TEM). *Conference Proceedings from the 39th International Symposium for Testing and Failure Analysis* (ed. Lucko, J.) 236–238 (ASM International, San Jose, CA, USA, 2013).
- 21 Pirovano, A., Lacaíta, A. L., Benvenuti, A., Pellizzer, F., Hudgens, S. & Bez, R. Scaling analysis of phase-change memory technology. *IEEE IEDM Tech. Dig.* **29**, 1–4 (2003).
- 22 Suh, D. S., Kim, C., Kim, K. H. P., Kang, Y. S., Lee, T. Y., Khang, Y., Park, T. S., Yoon, Y. G., Im, J. & Ihm, J. Thermoelectric heating of  $\text{Ge}_2\text{Sb}_2\text{Te}_5$  in phase change memory devices. *Appl. Phys. Lett.* **96**, 123115 (2010).
- 23 Lal, K., Meikap, A. K., Chattopadhyay, S. K., Chatterjee, S. K., Ghosh, M., Baba, K. & Hatada, R. Electrical resistivity of titanium nitride thin films prepared by ion beam-assisted deposition. *Phys. B* **307**, 150–157 (2001).
- 24 Kim, D. H., Merget, F., Forst, M. & Kurz, H. Three-dimensional simulation model of switching dynamics in phase change random access memory cells. *J. Appl. Phys.* **101**, 083538 (2007).
- 25 Kim, D. H., Merget, F., Laurenzis, M., Bolivar, P. H. & Kurz, H. Electrical percolation characteristics of  $\text{Ge}_2\text{Sb}_2\text{Te}_5$  and Sn doped  $\text{Ge}_2\text{Sb}_2\text{Te}_5$  thin films during the amorphous to crystalline phase transition. *J. Appl. Phys.* **97** (2005).
- 26 Ielmini, D. & Zhang, Y. G. Analytical model for subthreshold conduction and threshold switching in chalcogenide-based memory devices. *J. Appl. Phys.* **102**, 054517 (2007).

- 27 Hudgens, S. Progress in understanding the Ovshinsky effect: threshold switching in chalcogenide amorphous semiconductors. *Phys. Status Solidi B* **249**, 1951–1955 (2012).
- 28 Nardone, M., Karpov, V. G., Jackson, D. C. S. & Karpov, I. V. A unified model of nucleation switching. *Appl. Phys. Lett.* **94**, 103509 (2009).
- 29 Ielmini, D. Threshold switching mechanism by high-field energy gain in the hopping transport of chalcogenide glasses. *Phys. Rev. B* **78**, 035308 (2008).
- 30 Xiong, F., Liao, A. D., Estrada, D. & Pop, E. Low-power switching of phase-change materials with carbon nanotube electrodes. *Science* **332**, 568–570 (2011).
- 31 Nardone, M., Karpov, V. G. & Karpov, I. V. Relaxation oscillations in chalcogenide phase change memory. *J. Appl. Phys.* **107**, 054519 (2010).
- 32 Yamada, N. & Matsunaga, T. Structure of laser-crystallized  $\text{Ge}_2\text{Sb}_{2+x}\text{Te}_5$  sputtered thin films for use in optical memory. *J. Appl. Phys.* **88**, 7020–7028 (2000).
- 33 Wamwangi, D., Njoroge, W. K. & Wuttig, M. Crystallization kinetics of  $\text{Ge}_4\text{Sb}_1\text{Te}_5$  films. *Thin Solid Films* **408**, 310–315 (2002).
- 34 Kaiser, M., van Pieteron, L. & Verheijen, M. A. *In situ* transmission electron microscopy analysis of electron beam induced crystallization of amorphous marks in phase-change materials. *J. Appl. Phys.* **96**, 3193–3198 (2004).
- 35 Jung, Y., Nam, S. W. & Agarwal, R. High-resolution transmission electron microscopy study of electrically-driven reversible phase change in  $\text{Ge}_2\text{Sb}_2\text{Te}_5$  nanowires. *Nano Lett.* **11**, 1364–1368 (2011).
- 36 Kalb, J., Spaepen, F., Leervad Pedersen, T. & Wuttig, M. Viscosity and elastic constants of thin films of amorphous Te alloys used for optical data storage. *J. Appl. Phys.* **94**, 4908–4912 (2003).
- 37 Padilla, A., Burr, G. W., Virwani, K., Debnunne, A., Rettner, C. T., Topuria, T., Rice, P. M., Jackson, B., Dupouy, D., Kellock, A. J., Shelby, R. M., Gopalakrishnan, K., Shenoy, R. S. & Kurdi, B. N. Voltage polarity effects in GST-based phase change memory: physical origins and implications. *IEEE IEDM Tech. Dig.* **29**, 1–4 (2010).
- 38 Legendre, B., Hancheng, C., Bordas, S. & Clavaguera-Mora, M. T. Phase diagram of the ternary system Ge-Sb-Te. I. The subternary Ge-Te-Sb<sub>2</sub>Te<sub>3</sub>-Te. *Thermochim. Acta* **78**, 141 (1984).
- 39 Bordas, S., Clavaguera-Mora, M. T., Legendre, B. & Hancheng, C. Phase diagram of the ternary system Ge-Sb-Te. II. The subternary Ge-GeTe-Sb<sub>2</sub>Te<sub>3</sub>-Sb. *Thermochim. Acta* **107**, 239 (1986).



This work is licensed under a Creative Commons Attribution 4.0 International License. The images or other third party material in this article are included in the article's Creative Commons license, unless indicated otherwise in the credit line; if the material is not included under the Creative Commons license, users will need to obtain permission from the license holder to reproduce the material. To view a copy of this license, visit <http://creativecommons.org/licenses/by/4.0/>

Supplementary Information accompanies the paper on the NPG Asia Materials website (<http://www.nature.com/am>)